



Ultrafast polarization control in κ -(BEDT-TTF) $_2X$

Shu Ohmura , Jun Tokimoto , and Akira Takahashi

Department of Physics and Engineering, Nagoya Institute of Technology, Gokiso-Cho, Showa-ku, Nagoya 466-8555, Japan



(Received 31 March 2021; revised 27 August 2021; accepted 9 September 2021; published 5 October 2021)

We present a theoretical investigation of the dynamics induced by higher-frequency off-resonant light pulse excitation in the metallic phase of κ -(BEDT-TTF) $_2X$ [where BEDT-TTF is bis(ethylenedithio)-tetrathiafulvalene and X represents a counteranion] by solving the time-dependent Schrödinger equation numerically in the quarter-filled extended Hubbard model for the material. If the magnitude of the applied light pulse exceeds a critical value, the transition to the charge-ordered (CO) state is then induced by the light pulse excitation. In the CO state, one site forming a dimer becomes charge rich, the other site becomes charge poor, and the intradimer electric dipole moments are aligned in a particular direction. The transition is driven by photoinduced reduction of the effective transfer integrals and can therefore be regarded as a dynamical localization-related phenomenon. There are two degenerate A phase and B phase CO states that have opposite polarization directions. The photogenerated CO state is given by the superposition of the A phase and B phase CO states with equal weights, and the polarization of the photogenerated CO state is effectively zero. Transitions to either of the two polarized CO states can be induced selectively, and the polarization can be generated by excitation using light and terahertz pulses. Furthermore, the polarization can be reversed on a timescale of several tens of femtoseconds by excitation using double light and terahertz pulses, which induce the following phase transitions: metal \rightarrow polarized CO state of the A (B) phase \rightarrow metal \rightarrow polarized CO state of the B (A) phase \rightarrow metal.

DOI: [10.1103/PhysRevB.104.134302](https://doi.org/10.1103/PhysRevB.104.134302)

I. INTRODUCTION

Ferroelectric materials are used in a wide variety of devices, including random access memory circuits, capacitors, sensors, piezoelectric actuators, and optical devices [1–3]. If the ferroelectric polarization could be controlled on a picosecond-level timescale, ferroelectric materials could then be used to form advanced switching devices. However, in conventional ferroelectric materials, the electric polarization is governed by the rotation of polar molecules or by the displacement of ions, and the typical time constants for the polarization vary in length from micro- to milliseconds.

Recently, ferroelectricity that arises from electron transfer, which is called electronic ferroelectricity [4–6], has been observed in various materials, including multiferroics [7–14], transition metal oxides [15–17], and organic molecular compounds [18–37], and much faster polarization switching is expected to be enabled by this new type of ferroelectricity.

Ultrashort terahertz (THz) pulses have proven to be powerful tools for investigation of ultrafast dielectric responses because of their strongly asymmetric electric field wave forms, which have one dominant half cycle. THz-pump optical probe measurements and second-harmonic-generation (SHG) probe measurements have revealed the instantaneous response of the charge and the electronic contribution to the polarization (i.e., the electronic polarization) in the electronic ferroelectrics tetrathiafulvalene-*p*-chloranil (TTF-CA) [38] and α -(BEDT-TTF) $_2X$ [where BEDT-TTF is bis(ethylenedithio)-tetrathiafulvalene and X is a counteranion] [39]. Furthermore, it has been demonstrated theoretically

that these instantaneous responses originate from the adiabatic nature of the THz pulse excited state [40,41].

The research above has focused on small changes in the charge structure and the electronic polarization. Recently, it was shown experimentally that large changes can be induced in the electronic polarization of a variety of materials by high-intensity THz pulse excitation. The magnitude of the polarization was increased to approximately 20% of that in the ferroelectric ionic phase in the paraelectric neutral phase of TTF-CA [42], a transition from a Mott insulator to a macroscopically polarized charge-ordered (CO) state was induced in κ -(BEDT-TTF) $_2\text{Cu}[\text{N}(\text{CN})_2]\text{Cl}$ [43], and ferroelectricity was induced in the quantum paraelectric material SrTiO $_3$ [44,45]. However, ultrafast polarization reversal, which is required for advanced device applications, has not been observed to date among these experimental investigations. A theoretical study showed that the polarization can be reversed on a picosecond timescale by high-intensity THz pulse excitation in TTF-CA near the phase boundary between its ionic and neutral phases [46]. However, this polarization reversal is driven by collective lattice motion triggered by the pulse excitation and cannot be controlled using the pulse.

To meet the challenge of realizing ultrafast polarization reversal, we present an approach that uses photoinduced phase transitions. Photoinduced phase transitions [47–51] have been observed in several different materials, and the investigation of the phenomenon is expected to lead to ultrafast control of the material phases and the discovery of new nonequilibrium phases. Most of the transitions investigated to date have been oriented toward destruction of the order of the ground state, but photoinduced phenomena oriented in the reverse

direction were observed recently. The electronic order of a charge density wave [52–54], spin density waves [55], superconductivity [56–58], ferroelectricity [34], and the charge order [59–63] have all been reported to be enhanced by photoexcitation.

Among these photoinduced phase transitions in the reverse direction, we consider those that are the result of dynamical localization [64–66]. If the time period of the light is much smaller than the characteristic timescale of the electron motion, the electrons will then respond approximately to the effective transfer integrals, which are given by the time averages of the photomodulated transfer integrals. Under strong excitation, the magnitudes of the effective transfer integrals are reduced significantly by light excitation. The correlated phases are stabilized, and the transition from a metallic state to a correlated state may be induced by this reduction. The dynamical localization was originally proposed to occur under continuous light excitation. However, if the pulse duration is sufficiently long, the localization that occurs as a result of the reduction in the effective transfer integral magnitudes is also induced through pulse excitation. Therefore, we hereafter refer to the localization induced by pulse excitation as dynamical localization. The reduction of the transfer integral has been observed as a redshift in the plasmlike reflectivity edge in $(\text{TMTTF})_2\text{AsF}_6$ (where TMTTF is tetramethyltetrafulvalene) [67]. Furthermore, recent pump-probe spectroscopy experiments showed that a short-range charge order is induced by intense infrared pulse excitation from the metallic phase of $\alpha\text{-(BEDT-TTF)}_2\text{I}_3$ immediately above the transition temperature [62,63], and localization of the electrons has been proposed to be the result of dynamical localization-related effects cooperating with the Coulomb interaction and the characteristic lattice structure of the compound [68,69]. The photoinduced transitions to the CO phases have been demonstrated theoretically in the high-intensity excitation case [70].

There have been rapid developments in correlated systems far from equilibrium that are driven using strong alternating current electric fields [71–76]. Dynamical localization is a representative example of the exotic phenomena realized in these systems. This proposed mechanism for the photoinduced transition is essentially different from that of the conventional photoinduced phase transition. Because of the uncertainty relation between energy and time, the electronic system can be excited by off-resonant light, but the lifetime of the photoexcited state is approximately $\hbar/|\Delta E|$, where ΔE is the difference between the photon energy and the excitation energy of the state. The mechanisms of the photoinduced phase transitions are dependent on the lifetime. In conventional photoinduced phase transitions, local change in the electronic structure is initially induced by photoexcitation; collective motions of the electrons and/or phonons are then driven by the local change, and these collective motions result in a macroscopic excited domain with electronic and/or lattice orders that differ from the order of the ground state. This type of photoinduced phase transition can be regarded as the result of real excitation because it occurs only when $|\Delta E|$ is so small that the lifetime of the photoexcited state is longer than the typical timescales of the electron and/or lattice motions. Different types of transition can then be induced by the off-resonant light when the photoexcited state's lifetime

is shorter than the typical timescales of the electron and lattice motions. One representative example is the photoinduced phase transition due to dynamical localization. In this type of photoinduced phase transition, the photoinduced state is a light dressed state and exists only when the light pulse is on. We refer to this type of photoinduced phase transition as being caused by virtual excitation.

In this paper, we consider ultrafast control of the polarization in $\kappa\text{-(BEDT-TTF)}_2X$. $(\text{BEDT-TTF})_2X$ can be described as a quasi-two-dimensional strongly correlated electron system with a quarter-filled valence band in terms of holes. In $\kappa\text{-(BEDT-TTF)}_2X$, the BEDT-TTF molecular lattice is distorted to form dimers, and the hole orbitals of the two dimerized molecules are strongly hybridized. As a result, the dimers can effectively be treated as single sites, and $\kappa\text{-(BEDT-TTF)}_2X$ can be regarded as a half-filled system. $\kappa\text{-(BEDT-TTF)}_2X$ exhibits a Mott insulator phase if the Coulomb interaction energy between the two holes in a dimer exceeds its critical value [77–80]. This type of insulating state is called the dimer Mott insulator.

Recently, a dielectric anomaly was observed in the dimer Mott insulator $\kappa\text{-(BEDT-TTF)}_2\text{Cu}_2(\text{CN})_3$ [29], which indicates that the charge degrees of freedom are still active, in contrast to those in conventional Mott insulators. The origin of this dielectric anomaly has been researched intensively, and it has been proposed that the anomaly arises from the electric dipoles in the dimers [29–32,34,35]. It was demonstrated theoretically that the charge fluctuations are strongly enhanced near the phase boundary between the dimer Mott insulator and the ferroelectric CO phase, where one site in a dimer is charge rich and the other site is charge poor, and the dielectric anomaly can then be attributed to the charge fluctuation [30,36]. The CO state is an electronic ferroelectric state, and the dielectric anomaly indicates the possibility of electronic ferroelectricity in $\kappa\text{-(BEDT-TTF)}_2X$. Nevertheless, experimental results have been presented that indicate the absence of electric dipoles in dimers, where the origin of the dielectric anomaly has been attributed to magnetic domain walls coupled with charges [81–85]. The question of whether the electric dipoles in these dimers actually exist remains controversial.

In this paper, we propose an approach to ultrafast polarization control using the photoinduced phase transition to the CO state that results from dynamical localization in $\kappa\text{-(BEDT-TTF)}_2X$. We demonstrate numerically that a high-intensity, higher-frequency off-resonant light pulse can induce the transition from the metallic ground state to the CO state. The photogenerated CO state is given by the superposition of two degenerate CO states that have opposite polarizations, and this state therefore has no polarization. By applying a second strong THz pulse along with the light pulse, one of the two degenerate CO states can be generated selectively, and large polarizations can be generated. Furthermore, by performing excitation using double pulses, we can reverse and control the polarization on a timescale of 100 fs.

II. THEORY

Consider the two-dimensional quarter-filled extended Hubbard Hamiltonian for holes given by

$$H(t) = \sum_{\langle n,m \rangle, \sigma} [\beta_{n,m}(t) c_{n,\sigma}^\dagger c_{m,\sigma} + \text{H.c.}] + U \sum_n n_{n,\uparrow} n_{n,\downarrow} + \sum_{\langle n,m \rangle} V_{n,m} n_n n_m. \quad (1)$$

The first term represents the transfer of the holes, where $\sum_{\langle n,m \rangle}$ denotes a sum over neighboring site pairs, $c_{n,\sigma}^\dagger$ ($c_{n,\sigma}$) is the creation (annihilation) operator for the hole with spin σ at site n , and $\beta_{n,m}(t)$ is the transfer integral between sites n and m at time t . The second and third terms represent the on-site Coulomb interaction and the Coulomb interaction between neighboring sites, respectively, where U is the on-site Coulomb interaction energy, $n_{n,\sigma} = c_{n,\sigma}^\dagger c_{n,\sigma}$, $V_{n,m}$ is the Coulomb interaction energy between neighboring sites n and m , and $n_n = \sum_\sigma n_{n,\sigma}$. The electron-light interaction is introduced by the Peierls phase as

$$\beta_{n,m}(t) = \beta_{n,m}^{(0)} \exp[i\mathbf{A}(t) \cdot (\mathbf{r}_n - \mathbf{r}_m)], \quad (2)$$

where $\beta_{n,m}^{(0)}$ is the transfer integral between neighboring sites n and m under zero field, $\mathbf{A}(t)$ is the vector potential of the applied field, and \mathbf{r}_n is the position vector of site n . We adopt atomic units, such that the velocity of light, the elementary electric charge, and \hbar are all equal to 1 throughout this paper. The field $\mathbf{A}(t)$ is assumed to be linearly polarized and has a Gaussian profile given by

$$\mathbf{A}(t) = A^{(\max)} \mathbf{e} \exp\left[-\left(\frac{t}{D}\right)^2\right] \cos(\omega t), \quad (3)$$

where $A^{(\max)}$ is the maximum amplitude of $\mathbf{A}(t)$, \mathbf{e} is the unit polarization vector, D is the pulse duration time, and ω is the optical frequency.

We consider an effective Hamiltonian for the higher-frequency off-resonant excitation case here, where $T = 2\pi/\omega$ is much smaller than the characteristic timescale for the hole motions. The holes then respond approximately to the effective transfer integrals, which are given by the following time-averaged transfer integral:

$$\bar{\beta}_{n,m}(t) = \frac{1}{T} \int_{t-T/2}^{t+T/2} \beta_{n,m}(\tau) d\tau. \quad (4)$$

If $D \gg T$ holds, then $\bar{\beta}_{n,m}(t)$ can be approximated as

$$\bar{\beta}_{n,m}(t) = \beta_{n,m}^{(0)} J_0 \left[|A^{(\max)}| \exp\left\{-\left(\frac{t}{D}\right)^2\right\} \mathbf{e} \cdot (\mathbf{r}_n - \mathbf{r}_m) \right], \quad (5)$$

where $J_0(x)$ is the Bessel function of order zero. The fraction $|\bar{\beta}_{n,m}(0)|/|\beta_{n,m}^{(0)}|$ at the pulse peak is a decreasing function of $|A^{(\max)}|$, and its value approaches zero at around $|A^{(\max)}| = 2.4/|\mathbf{e} \cdot (\mathbf{r}_n - \mathbf{r}_m)|$. This reduction of the effective transfer integral magnitudes enhances the correlation effects and may then induce the transition from the metallic ground state to strongly correlated phases such as the dimer Mott insulator and the CO states. This is the mechanism of the photoinduced phase transition that results from dynamical localization.

To analyze the photoinduced dynamics, we solve the time-dependent Schrödinger equation (TDSE) numerically:

$$i \frac{\partial}{\partial t} |\psi(t)\rangle = H(t) |\psi(t)\rangle, \quad (6)$$

with the initial condition $|\psi(-\infty)\rangle = |\psi_0\rangle$, where $|\psi_0\rangle$ is the ground state of the electronic Hamiltonian H_e and H_e is given by $H(t)$ for $\mathbf{A}(t) = 0$.

To interpret the results, we consider the effective Hamiltonian $\bar{H}(t)$ that is obtained by replacing $\beta_{n,m}(t)$ in $H(t)$ with $\bar{\beta}_{n,m}(t)$,

$$\bar{H}(t) = \sum_{\langle n,m \rangle, \sigma} \bar{\beta}_{n,m}(t) (c_{n,\sigma}^\dagger c_{m,\sigma} + \text{H.c.}) + U \sum_n n_{n,\uparrow} n_{n,\downarrow} + \sum_{\langle n,m \rangle} V_{n,m} n_n n_m, \quad (7)$$

and calculate the dynamics that result from the effective Hamiltonian numerically:

$$i \frac{\partial}{\partial t} |\bar{\psi}(t)\rangle = \bar{H}(t) |\bar{\psi}(t)\rangle, \quad (8)$$

with the same initial condition of $|\bar{\psi}(-\infty)\rangle = |\psi_0\rangle$. The eigenequation for the effective Hamiltonian is

$$\bar{H}(t) |\phi_0(t)\rangle = E_0(t) |\phi_0(t)\rangle, \quad (9)$$

where $|\phi_0(t)\rangle$ and $E_0(t)$ are the ground state of $\bar{H}(t)$ and its energy eigenvalue, respectively, and this eigenequation is also solved numerically. If $\bar{H}(t)$ is valid as an effective Hamiltonian for consideration of the photoinduced dynamics, then $|\bar{\psi}(t)\rangle \approx |\psi(t)\rangle$ holds for all t . Furthermore, $|\psi(t)\rangle \approx |\phi_0(t)\rangle$ holds if the photoinduced dynamics are adiabatic.

We solve the TDSE by discretizing time and using a finite-order Taylor expansion; that is, we approximate the time evolution operator over the time period from t to $t + \Delta t$ as

$$U(t + \Delta t, t) = \sum_{p=0}^P \frac{1}{p!} \left\{ -i\Delta t H \left(t + \frac{\Delta t}{2} \right) \right\}^p. \quad (10)$$

The highest-order P of the Taylor expansion is determined such that the norm of the highest-order contribution, which is given by

$$\frac{1}{p!} \left\{ -i\Delta t H \left(t + \frac{\Delta t}{2} \right) \right\}^p |\psi(t)\rangle, \quad (11)$$

is smaller than the tolerance ϵ . In the numerical calculations presented in this paper, the following parameters are used: $\Delta t = 0.03$ and $\epsilon = 10^{-15}$. Hereafter, we use eV as the unit of energy and eV^{-1} as the unit of time, where 1 eV^{-1} is equal to 0.66 fs. The numerical errors due to the use of this approximation in the various calculated physical quantities were estimated based on the differences between their values when calculated with $\Delta t = 0.03$ and 0.045 and with $\epsilon = 10^{-15}$ and 10^{-14} . The numerical values obtained when using the different Δt or ϵ values are indistinguishable graphically in the figures presented in this paper. For example, the differences between the charge correlation functions obtained for $\Delta t = 0.03$ and 0.045 and the differences between those obtained for $\epsilon = 10^{-15}$ and 10^{-14} are both less than 2×10^{-7} . The time evolution is calculated using the same method with a much longer simulation time of approximately 10 000 in the THz-pulse-induced neutral-ionic transition in TTF-CA [46], and the numerical errors in the physical quantity considered, e.g., the charge density, are not visible in the graphs. This

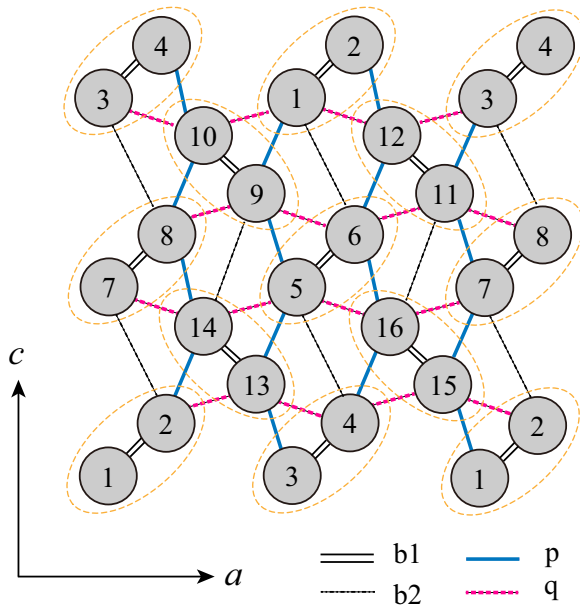


FIG. 1. Lattice structure of κ -(BEDT-TTF) $_2$ X. Orange ellipses indicate the dimers.

method can be used for simulations with simulation times of approximately 10 000 or longer.

III. RESULTS

A 4×4 cluster (system size $N = 16$) with a periodic boundary condition is used, and each site is numbered as shown in Fig. 1. We use the crystal axes for κ -(BEDT-TTF) $_2$ Cu[N(CN) $_2$]Cl. There are four nonequivalent bonds, which are labeled b1, b2, p, and q according to the method of Mori *et al.* [86]. From this point, the neighboring site pair (n, m) is denoted by its bond name, as indicated in Fig. 1. The b1 bond is the strongest bond and forms the dimers. We used the following transfer integrals: $\beta_{b1}^{(0)} = 0.265$, $\beta_{b2}^{(0)} = 0.098$, $\beta_p^{(0)} = 0.109$, and $\beta_q^{(0)} = -0.038$, which were calculated using the extended Hückel method for κ -(BEDT-TTF) $_2$ Cu[N(CN) $_2$]Br [86]. We also used the following Coulomb interaction energies: $U = 0.70$, $V_{b1} = 0.45$, $V_{b2} = V_p = 0.25$, and $V_q = 0.20$. Because the q bonds are significantly longer than the other interdimer bonds, we use the smaller value for V_q . The validity of the Coulomb parameters is discussed in Ref. [37]. The ground state $|\psi_0\rangle$ of the electronic Hamiltonian H_e is calculated using the Lanczos method, and this set of parameters gives the metallic ground state. The position vectors \mathbf{r}_n are determined using the following parameters [86]: the lattice constant along the a axis is 12.9 Å, the corresponding constant along the c axis is 8.4 Å, the dihedral angle between the molecular planes is 92.3°, the inclination angle of the molecular long axis is 34.0° from the direction oriented perpendicular to the conducting sheet, and the distance between the molecules in a dimer is 3.56 Å.

We calculate the light absorption spectrum $\alpha(\omega)$ for the metallic ground state $|\psi_0\rangle$ using the Lanczos method, and $\alpha(\omega)$ is shown in Fig. 2. A small peak occurs around $\omega = 0$, while large peaks exist around $\omega = 0.3$. These features agree with those of the experimentally obtained absorption

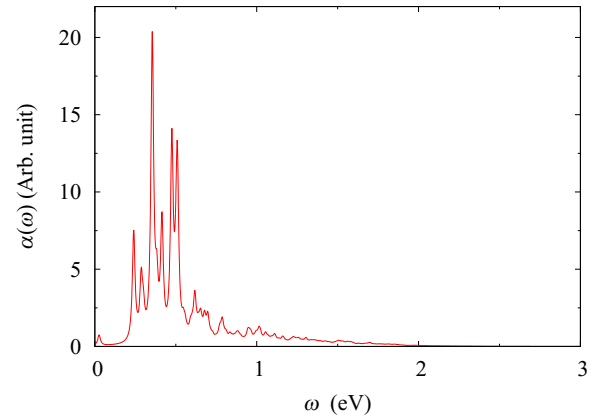


FIG. 2. Light absorption spectrum $\alpha(\omega)$. An artificial broadening of 0.01 is used.

spectrum [87,88]. The spectrum $\alpha(\omega)$ is almost zero, and the off-resonant condition is satisfied for values of $\omega > 2.5$.

A. Photoinduced transition to CO phase

We consider the dynamics for $A^{(\max)} = 0.8 \text{ \AA}^{-1}$, where \mathbf{e} points in the positive a -axis direction ($\mathbf{e} \parallel a$), $D = 60$, and $\omega = 2.5$, which is in the higher-frequency off-resonant and intense excitation case. The dependence of the dynamics on ω and $A^{(\max)}$ will be demonstrated later. This light parameter set gives the maximum amplitude of the electric field as $E^{(\max)} = 2.0 \times 10^8 \text{ V/cm}$. To investigate the physical properties of the solution $|\psi(t)\rangle$ to the TDSE, we consider the overlap $S(t) \equiv |\langle \psi_0 | \psi(t) \rangle|^2$ and the probability $W_s(t)$ that a dimer is singly occupied for $|\psi(t)\rangle$. The solution $|\psi(t)\rangle$ is expressed as a linear combination of many basis states. The probability $W_s(t)$ is given by the sum of the weights of the basis states that have a single hole in a given dimer. Note that $W_s(t)$ is independent of the chosen dimer because all the dimers are equivalent. The probability $W_s(t)$ indicates the magnitude of the correlation effect; $W_s = 0.5$ holds if there is no correlation effect and the holes are distributed randomly, and $W_s = 1$ holds in the strong on-dimer Coulomb interaction case. The corresponding probability for the dimer Mott insulator ground state ($W_s^{(\text{DMI})}$) is approximately 0.85 near the boundary with the metallic phase, and the probability for the present metallic ground state ($W_s^{(\text{M})}$) is 0.72. We also consider the weights of the metallic states for $|\psi(t)\rangle$ defined by $W_m(t) \equiv \sum_{l=1}^{16} |\langle \psi_l^{(\text{M})} | \psi(t) \rangle|^2$, where $|\psi_l^{(\text{M})}\rangle$ are 16 degenerate metallic ground states in the noninteracting case where $U = 0$ and $V_{b1} = V_{b2} = V_p = V_q = 0$. The weight for the metallic ground state $|\psi_0\rangle$ ($W_m^{(\text{M})} \equiv \sum_{l=1}^{16} |\langle \psi_l^{(\text{M})} | \psi_0 \rangle|^2$) is 0.55, demonstrating that the metallic states have a major weight in $|\psi_0\rangle$. This weight is smaller than 1 as a result of correlation effects. If the holes are localized in $|\psi(t)\rangle$ because of a strong correlation effect, $W_m(t)$ is then effectively zero. In fact, the weight for the dimer Mott insulator state is effectively zero. The metallic nature of $|\psi(t)\rangle$ can be seen from $W_m(t)$.

We show the time variations of $W_s(t)$, $W_m(t)$, and $S(t)$ in Fig. 3. $W_s(t)$ initially increases and becomes greater than $W_s^{(\text{DMI})}$ for $-30 \lesssim t \lesssim 30$. This large $W_s(t)$ indicates that the photogenerated state is a strongly correlated state. $S(t)$ and

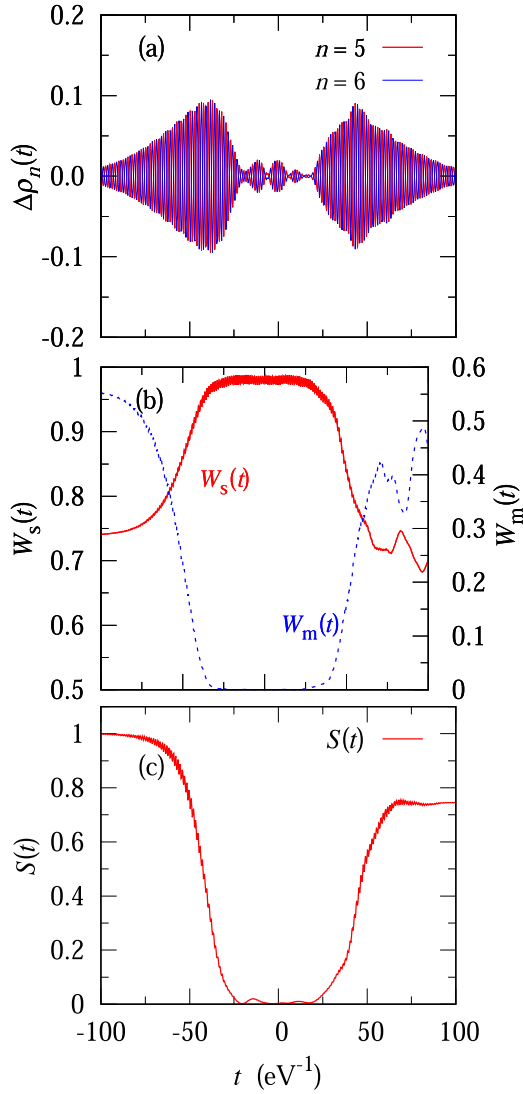


FIG. 3. Temporal variations of (a) $\Delta\rho_n(t)$, (b) $W_s(t)$ and $W_m(t)$, and (c) $S(t)$ for $A^{(\max)} = 0.8 \text{ \AA}^{-1}$, $e \parallel a$, $D = 60$, and $\omega = 2.5$.

$W_m(t)$ are both reduced drastically by photoexcitation and almost reach zero within the time range $-30 \lesssim t \lesssim 30$, during which the strongly correlated state is photogenerated. These results show that the photogenerated state has effectively no overlap with the metallic ground state and the dynamics can thus be regarded as a photoinduced phase transition. After the pulse is turned off, $S(t)$ becomes close to 1, thus showing that $|\psi(t)\rangle$ has a major overlap with the ground state, even in the intense excitation case.

To investigate the photoinduced strongly correlated phase, we calculated the photoinduced charge at site n :

$$\Delta\rho_n(t) = \rho_n(t) - 0.5, \quad (12)$$

where $\rho_n(t)$ is the charge at site n and is given by

$$\rho_n(t) = \langle \psi(t) | n_n | \psi(t) \rangle, \quad (13)$$

and we use the facts that all sites are equivalent in the electronic Hamiltonian H_e and the charge for the ground state is 0.5 at all sites. The charge correlation $\xi_{n,m}(t)$ between sites n

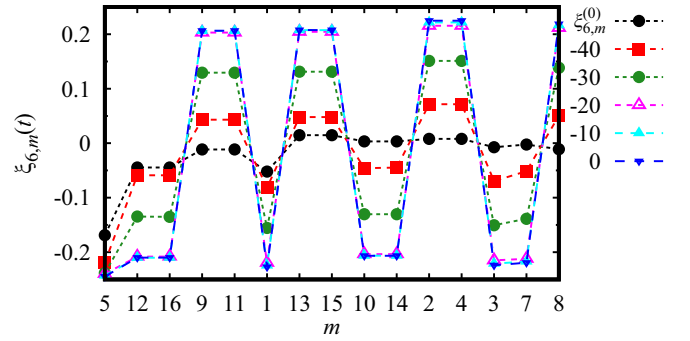


FIG. 4. Charge correlations $\xi_{6,m}^{(0)}$ for the ground state and the correlations $\xi_{6,m}(t)$ for $|\psi(t)\rangle$ at $t = -40, -30, -20, -10$, and 0 when $A^{(\max)} = 0.8 \text{ \AA}^{-1}$, $e \parallel a$, $D = 60$, and $\omega = 2.5$.

and m is defined by

$$\xi_{n,m}(t) = \langle \psi(t) | [n_n - \rho_n(t)][n_m - \rho_m(t)] | \psi(t) \rangle. \quad (14)$$

The charge correlations $\xi_{6,m}$ at $t = -40, -30, -20, -10$, and 0 are shown in Fig. 4. Within the time range $-30 \lesssim t \lesssim 30$, during which the transient strongly correlated state is photogenerated, the values of $|\xi_{6,m}|$ become much greater than the corresponding values for the ground state $|\xi_{6,m}^{(0)}|$. The charge correlations $\xi_{n,m}$ between the red sites in Fig. 5 and the correlations between the gray sites are positive, but the correlations between the red and gray sites are negative. Furthermore, the correlations $|\xi_{n,m}|$ are almost independent of the distances between the site pairs and are close to the maximum value of 0.25. Note that the correlations $|\xi_{n,m}|$ for the CO state are maximal in the absence of charge fluctuations and they have a maximum value of 0.25. These strong long-range charge correlations show that the photoinduced strongly correlated state is a CO state, and the charge order

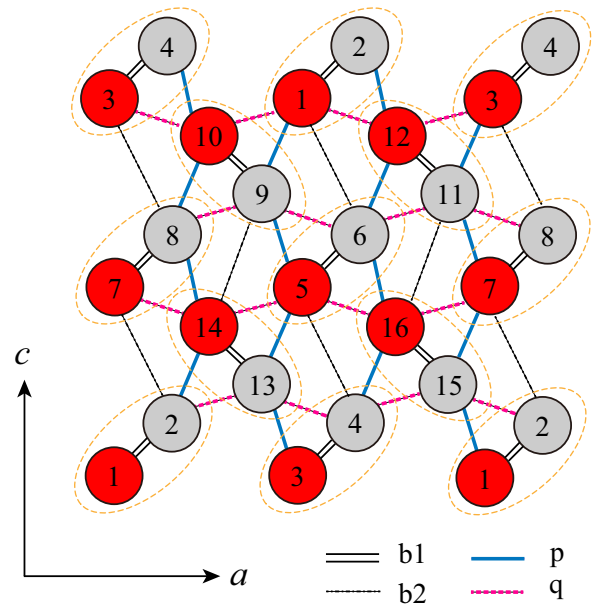


FIG. 5. Charge order pattern for the CO state. The red sites are charge rich (charge poor), and the gray sites are charge poor (charge rich) in the A (B) phase CO state.

pattern of the CO state is illustrated schematically in Fig. 5. In the CO state, one site forming a dimer becomes charge rich while the other corresponding site becomes charge poor, and the intradimer electric dipole moments are then aligned along the a axis. There are two degenerate CO states, called the A phase and B phase CO states. The red (gray) sites in Fig. 5 are charge rich, and the gray (red) sites are charge poor in the A (B) phase CO state $|\phi_A^{(\text{CO})}\rangle$ ($|\phi_B^{(\text{CO})}\rangle$). The CO state $|\phi_A^{(\text{CO})}\rangle$ ($|\phi_B^{(\text{CO})}\rangle$) has polarization because of the electric dipoles in the dimers, and the polarization is oriented in the negative (positive) a -axis direction. Furthermore, because the electric dipole is generated by hole transfer within the dimer, the CO state is an electronic ferroelectric state.

We show the temporal variations in $\Delta\rho_n(t)$ in Fig. 3(a). Charge disproportionation does not occur in the dimer, and the polarization is effectively zero within the time range in which the CO states are photogenerated. This is because the photoinduced CO state $|\psi(t)\rangle$ is given approximately by superposition of $|\phi_A^{(\text{CO})}\rangle$ and $|\phi_B^{(\text{CO})}\rangle$ with equal weights.

B. dynamical localization

In this section, to investigate the origin of the photoinduced phase transition, we compare the charge correlations and the bond orders for the solution $|\psi(t)\rangle$ to the TDSE (6) with the original extended Hubbard Hamiltonian $H(t)$ with the corresponding quantities for the solution $|\bar{\psi}(t)\rangle$ to the TDSE (8) with the effective Hamiltonian $\bar{H}(t)$ in Figs. 6(a) and 6(b). The charge correlation $\xi_{n,m}(t)$ between sites n and m for $|\bar{\psi}(t)\rangle$ is defined by

$$\xi_{n,m}(t) = \langle \bar{\psi}(t) | [n_n - \bar{\rho}_n(t)] [n_m - \bar{\rho}_m(t)] | \bar{\psi}(t) \rangle, \quad (15)$$

$$\bar{\rho}_n(t) = \langle \bar{\psi}(t) | n_n | \bar{\psi}(t) \rangle. \quad (16)$$

The bond orders of the X bond, denoted by $p_X(t)$ and $\bar{p}_X(t)$ for $|\psi(t)\rangle$ and $|\bar{\psi}(t)\rangle$, respectively, are defined by

$$p_X(t) = \text{Re} \left[\sum_{\sigma} \langle \psi(t) | c_{n,\sigma}^{\dagger} c_{m,\sigma} | \psi(t) \rangle \right], \quad (17)$$

$$\bar{p}_X(t) = \text{Re} \left[\sum_{\sigma} \langle \bar{\psi}(t) | c_{n,\sigma}^{\dagger} c_{m,\sigma} | \bar{\psi}(t) \rangle \right], \quad (18)$$

where the X bond connects sites n and m . The absolute values of the charge correlations show the magnitude of the charge order, and the absolute values of the bond orders decrease as the electrons become more localized. Actually, during the time range $-30 \lesssim t \lesssim 30$ in which the CO states are photogenerated, $|p_X(t)|$ ($|\xi_{n,m}(t)|$) are much smaller (larger) than the corresponding values of the ground state. We can therefore see how the photoinduced phase transition proceeds from the time variations in $\xi_{n,m}(t)$ and $p_X(t)$.

The time variations in the various physical quantities caused by $\bar{H}(t)$, including $\xi_{n,m}(t)$ and $\bar{p}_X(t)$, are driven by the time variations of the effective transfer integrals $\bar{\beta}_X(t)$. If we ignore rapid and small oscillations, the values of $\xi_{n,m}(t)$ [$\bar{p}_X(t)$] are almost identical to those of $\xi_{n,m}$ [$p_X(t)$], which demonstrates that $|\psi(t)\rangle$ can be approximated very well using $|\bar{\psi}(t)\rangle$, and the transition can then be regarded as being

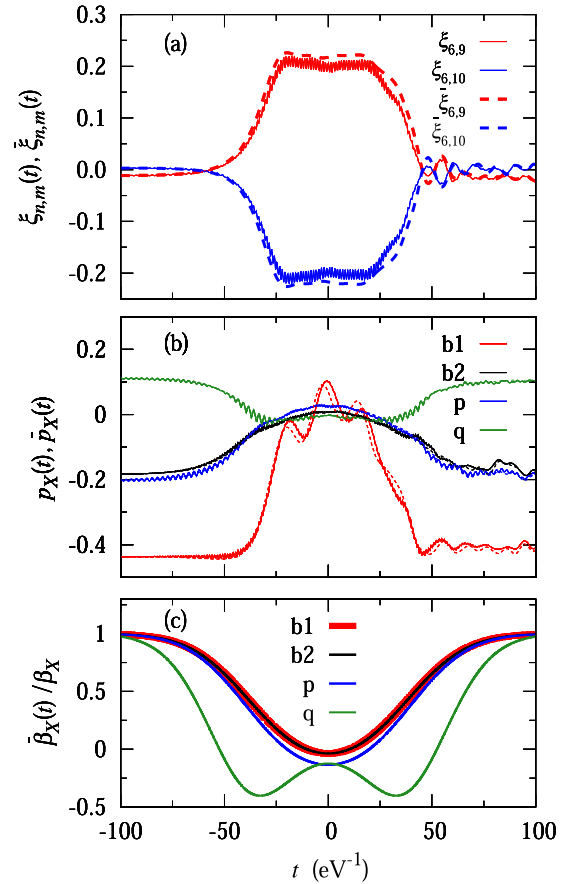


FIG. 6. Temporal variations in (a) $\xi_{n,m}(t)$ (solid lines) and $\bar{\xi}_{n,m}(t)$ (dashed lines), (b) $p_X(t)$ (solid lines) and $\bar{p}_X(t)$ (dashed lines), and (c) $\bar{\beta}_X(t)/\beta_X^{(0)}$ when $\mathbf{e} \parallel a$, $\omega = 2.5$, $A^{(\text{max})} = 0.8 \text{ \AA}^{-1}$, and $D = 60$.

induced by the time variations in the effective transition integrals.

We show the time variations in $\bar{\beta}_X(t)/\beta_X^{(0)}$ in Fig. 6(c). The magnitude of each effective transfer integral $|\bar{\beta}_X(t)|$ is reduced significantly from $|\beta_X^{(0)}|$ by photoexcitation within the time range in which the CO states are photogenerated. As $|\bar{\beta}_X(t)|$ decreases, $|p_X(t)|$ also decreases, and $|\xi_{n,m}(t)|$ increases. This strong correlation between $|\bar{\beta}_X(t)|$, $|\xi_{n,m}(t)|$, and $|p_X(t)|$ shows that the reduction in $|\bar{\beta}_X(t)|$ induces the localization of the electrons and enhances the charge order, which then results in the transition to the CO phase. Therefore, we can conclude that this transition is caused by dynamical localization.

We compare the weight of the metallic states $W_m(t)$ for $|\psi(t)\rangle$, that for $|\bar{\psi}(t)\rangle$ [$\bar{W}_m(t) \equiv \sum_{l=1}^{16} |\langle \psi_l^{(M)} | \bar{\psi}(t) \rangle|^2$], and that for $|\phi_0(t)\rangle$ [$W_m^{(0)}(t) \equiv \sum_{l=1}^{16} |\langle \psi_l^{(M)} | \phi_0(t) \rangle|^2$] around the transition point in Fig. 7. Both $W_m(t)$ and $\bar{W}_m(t)$ change continuously with time, but $W_m^{(0)}(t)$ changes discontinuously at $t = -47$. When t is regarded as a parameter in $\bar{H}(t)$, the crossing of the ground state occurs at $t = -47$, and the ground state of $\bar{H}(t)$ is the CO (metallic) state when $t > -47$ ($t < -47$). Therefore, the photoinduced transition is nonadiabatic, and the time required in this phase transition is of the order of tens of femtoseconds.

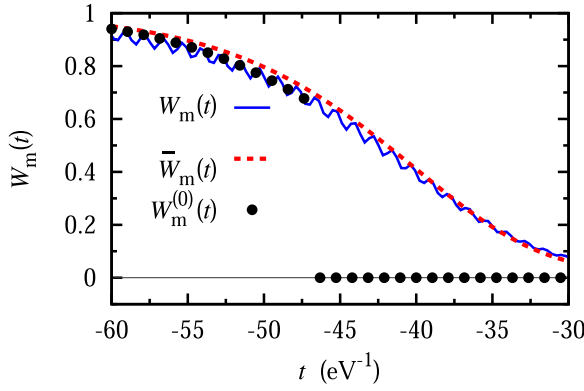


FIG. 7. Temporal variations of $W_m(t)$ (blue solid line), $\bar{W}_m(t)$ (red dashed line), and $W_m^{(0)}(t)$ (black dots) around the transition point for $A^{(\max)} = 0.8 \text{ \AA}^{-1}$, $e \parallel a$, $D = 60$, and $\omega = 2.5$.

Next, we investigate the ω and $A^{(\max)}$ dependences of the dynamics when numerically simulated using the TDSE given in (6). In Fig. 8(a), the ω dependence of $W_s(t)$ for $A^{(\max)} = 1 \text{ \AA}^{-1}$ is shown. When $\omega = 1$, $W_s(t)$ decreases gradually over time, and $W_s(t)$ is much smaller than the initial value $W_s^{(M)}$ after the pulse is turned off. In contrast, when $\omega \geq 2$, $W_s(t)$ shows the characteristic time variation of the transient photoinduced phase transition to the CO state. Furthermore, the temporal profile for $W_s(t)$ is almost independent of ω when $\omega \geq 2.5$. This is a characteristic feature of the photoinduced phase transition caused by dynamical localization because the effective transfer integrals $\bar{\beta}_X(t)$ are independent of ω in the higher-frequency off-resonant case, as shown by Eq. (5). In Fig. 8(b), the $A^{(\max)}$ dependence of $W_s(t)$ for $\omega = 2.5$ is shown. The transition to the CO state occurs for only the intense excitation case where $A^{(\max)} \geq 0.6 \text{ \AA}^{-1}$. These characteristic ω and $A^{(\max)}$ dependences show that the photoinduced phase transition occurs in the higher-frequency off-resonant and intense excitation case, which is consistent

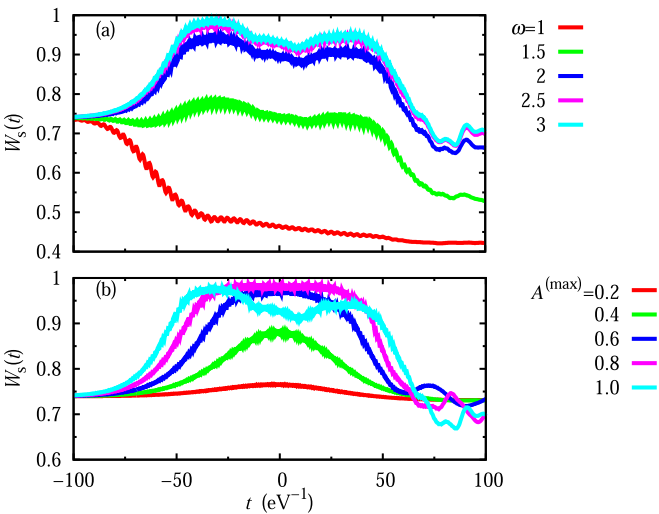


FIG. 8. (a) Temporal profiles of $W_s(t)$ for $A^{(\max)} = 1 \text{ \AA}^{-1}$ and $\omega = 1, 1.5, 2, 2.5,$ and 3 . (b) Corresponding profiles for $\omega = 2.5$ and $A^{(\max)} = 0.2, 0.4, 0.6,$ and 1 \AA^{-1} . For the other parameters, $e \parallel a$ and $D = 60$ are used.

with the conclusion that the transition is caused by dynamical localization.

In the virtual photoexcitation case, the photoexcited state exists only when the light pulse is on. As shown in Fig. 3(c), $S(t)$ does not return to 1 after photoexcitation, and this shows that the real photoexcitation cannot be ignored. After the light pulse has disappeared, only the effect of the real excitation remains in $|\psi(t)\rangle$. As seen from Fig. 6(a), the charge order is not increased in $|\psi(t)\rangle$ when compared with the ground state in the time region. The charge order is not enhanced by real excitation, and the CO phase is photogenerated in a transient manner.

In real photoexcitation cases, the photoinduced dynamics are caused by relaxation of the resonantly photoexcited initial states. Because these initial states differ, depending on the photon energy ω , the photoinduced dynamics are strongly dependent on ω . The time variance of $W_s(t)$ is strongly dependent on ω for values of $\omega < 2$, illustrating that the contribution of the real excitation is significant within this region. This is consistent with the fact that the light absorption spectrum extends to approximately 2. When $\omega < 2$, no increase is observed in $W_s(t)$, showing that the transition to the CO phase is prevented by the real excitation. The time variance of $W_s(t)$ is almost independent of ω when $\omega > 2.5$, i.e., where the transition to the CO phase occurs, as mentioned previously. This characteristic ω dependence of $W_s(t)$ confirms that the virtual excitation is dominant in inducing the phase transition.

There are two degenerate CO states that differ from A phase and B phase states, where one site forming a dimer becomes charge rich and the other site becomes charge poor, and the intradimer electric dipole moments are aligned along the c axis. We call these two degenerate states the C phase and D phase CO states. In the A phase and B phase (C phase and D phase) CO states, the charge-rich sites are connected via the q (p) bonds. Because V_p is greater than V_q , which is justified by the fact that the q bond is significantly longer than the p bond, the A phase and B phase CO states are more stable than the C phase and D phase states. This is the reason why the A phase and B phase CO states have the dominant weights in the photogenerated unpolarized CO state. With the exception of this point, which has a sensitive dependence on V_p and V_q , the conclusions presented in this paper remain unchanged if the electronic parameters are varied within a realistic range. The transition to the unpolarized CO state is also induced by c -axis polarized light pulse excitation. The photoinduced reduction in $|\bar{\beta}_X(t)|$ is dependent on the light polarization direction e , but the values of $|\bar{\beta}_X(t)|$ are also reduced significantly for all bonds in the intense excitation case for the c -axis polarized light pulse.

C. Polarization generation

To generate persistent and large polarization via light excitation, we need to generate either of the A phase or B phase CO states selectively. For this purpose, we consider the dynamics that occur when the irradiation includes a half-cycle THz pulse in addition to the higher-frequency off-resonant and intense light pulse. Ultrashort THz pulses can be approximated by the half-cycle pulse because the wave forms are strongly asymmetric, with one dominant half cycle. The

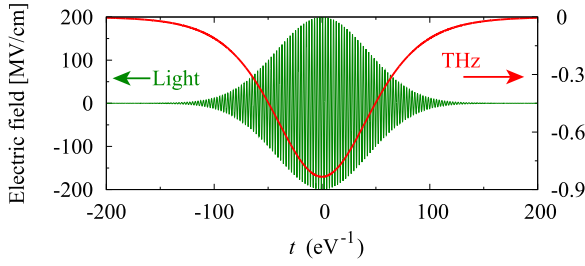


FIG. 9. Temporal profiles of electric fields of single light and THz pulses for $A_0^{(\max)} = 0.8 \text{ \AA}^{-1}$, $\mathbf{e}_0 \parallel a$, $D_0 = 60$, $\omega = 2.5$, $A_1^{(\max)} = 1.0 \text{ \AA}^{-1}$, $\mathbf{e}_1 \parallel a$, and $D_1 = 60$.

vector potential $\mathbf{A}(t)$ of these light and THz pulses is given by the following equation:

$$\mathbf{A}(t) = \mathbf{A}_0(t) + \mathbf{A}_1(t), \quad (19)$$

$$\mathbf{A}_0(t) = A_0^{(\max)} \mathbf{e}_0 \exp \left[-\left(\frac{t}{D_0} \right)^2 \right] \cos(\omega t), \quad (20)$$

$$\mathbf{A}_1(t) = A_1^{(\max)} \frac{1}{2} \mathbf{e}_1 \left[1 + \tanh \left(\frac{t}{D_1} \right) \right], \quad (21)$$

where $\mathbf{A}_0(t)$ [$\mathbf{A}_1(t)$] is the vector potential, $A_0^{(\max)}$ ($A_1^{(\max)}$) is the maximum amplitude, \mathbf{e}_0 (\mathbf{e}_1) is the unit polarization vector, D_0 (D_1) is the duration of the light (THz) pulse, and ω is the optical frequency. The subscript 0 (1) indicates the quantities for the light (THz) pulse.

We use the following parameters for the light pulse: $A_0^{(\max)} = 0.8 \text{ \AA}^{-1}$, $\mathbf{e}_0 \parallel a$, $D_0 = 60$, and $\omega = 2.5$. These parameters are used to calculate the photoinduced dynamics shown in Figs. 3, 4, 6, and 7. For the THz pulse, we use the following parameters: $A_1^{(\max)} = 1.0 \text{ \AA}^{-1}$, $\mathbf{e}_1 \parallel a$, $D_1 = 60$, for which we set the polarization direction of the THz pulse to match the polarization direction of the A phase and B phase CO states. The temporal profiles of the applied electric fields of the light and THz pulses are shown in Fig. 9.

The pulse excited state also has the characteristic charge correlation $\xi_{n,m}(t)$ from the A phase and B phase CO states when the pulses are on in this case. The temporal variations in $\Delta\rho_n(t)$ at sites 5 and 6, which form a dimer, are shown in Fig. 10. In contrast to the light pulse excited case, a persistent and large electric dipole moment is generated in the dimer when the pulses are on. Note that all red (gray) sites shown in Fig. 5 are equivalent to site 5 (6) in the present case, where both the light and THz pulses are polarized along the a direction. Therefore, the A phase CO state $|\phi_A^{(\text{CO})}\rangle$ has the dominant weight in $|\psi(t)\rangle$, and $|\psi(t)\rangle$ has polarization pointing along the negative a -axis direction. If the electric field is oriented in the opposite direction, the B phase CO state $|\phi_B^{(\text{CO})}\rangle$ then has the dominant weight, and the polarization of $|\psi(t)\rangle$ is in the opposite direction. We thus succeeded in selective polarization generation on a timescale of several tens of femtoseconds.

We have calculated the dynamic characteristics when the duration of the THz pulse is much shorter than that of the light pulse. For $D_1 \lesssim 10$, the THz pulse irradiation occurs after the transition to the CO state that effectively has zero polarization has been completed. The transition from the photogenerated

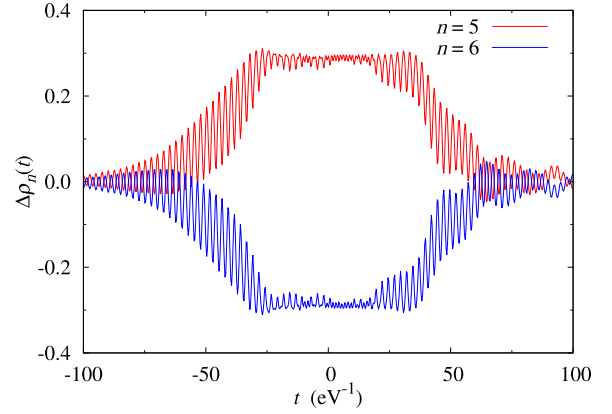


FIG. 10. Temporal variations in $\Delta\rho_n(t)$ for $n = 5$ and 6 induced by single light and THz pulses when $A_0^{(\max)} = 0.8 \text{ \AA}^{-1}$, $\mathbf{e}_0 \parallel a$, $D_0 = 60$, $\omega = 2.5$, $A_1^{(\max)} = 1.0 \text{ \AA}^{-1}$, $\mathbf{e}_1 \parallel a$, and $D_1 = 60$.

unpolarized CO state to the polarized CO state is not induced by the THz pulse within the realizable magnitude range considered in this paper. We have also calculated the dynamics induced by the light pulse and the THz double pulses with opposite electric field directions, the vector potential of which is given by

$$\begin{aligned} \mathbf{A}(t) = & A_0^{(\max)} \mathbf{e}_0 \exp \left[-\left(\frac{t}{D_0} \right)^2 \right] \cos(\omega_0 t) \\ & + \frac{A_1^{(\max)}}{2} \mathbf{e}_1 \tanh \left(\frac{t + d/2}{D_1} \right) \\ & - \frac{A_1^{(\max)}}{2} \mathbf{e}_1 \tanh \left(\frac{t - d/2}{D_1} \right), \end{aligned} \quad (22)$$

where d is the delay time between the first and second THz pulses. We use the smaller THz pulse duration $D_1 = 30$ and the delay time $d = 30$ to ensure that the two THz pulses are well separated and that they are radiated when the light pulse is on. Other than these parameters, we use the same parameters that were used to calculate the results shown in Fig. 10: $A_0^{(\max)} = 0.8 \text{ \AA}^{-1}$, $\mathbf{e}_0 \parallel a$, $D_0 = 60$, $\omega = 2.5$, $A_1^{(\max)} = 1.0 \text{ \AA}^{-1}$, and $\mathbf{e}_1 \parallel a$. The CO state with the large polarization is generated via excitation by the light pulse and the first THz pulse. However, the polarization is not reversed by the excitation by the second THz pulse, the electric field of which is oriented in the direction opposite to the polarization of the generated CO state. These results show that there is a high potential barrier between the A phase and B phase CO states, as shown schematically in Fig. 11. When the polarized CO state is generated, the polarization then cannot be reversed using a THz pulse with a realistic magnitude.

We have calculated the dynamics when the THz pulse is polarized along the c axis, and the temporal variations of $\Delta\rho_n(t)$ are shown in Fig. 12. The following parameters for the light and THz pulses are used: $A_0^{(\max)} = 0.8 \text{ \AA}^{-1}$, $\mathbf{e}_0 \parallel a$, $D_0 = 60$, $\omega = 2.5$, $A_1^{(\max)} = 1.0 \text{ \AA}^{-1}$, $\mathbf{e}_1 \parallel c$, and $D_1 = 60$. They are the same as those used to calculate the results shown in Fig. 10 except that $\mathbf{e}_1 \parallel c$ holds. The CO state that has the characteristic charge correlations of the A phase and B phase CO states is generated. Because \mathbf{e}_1 is oriented perpendicular

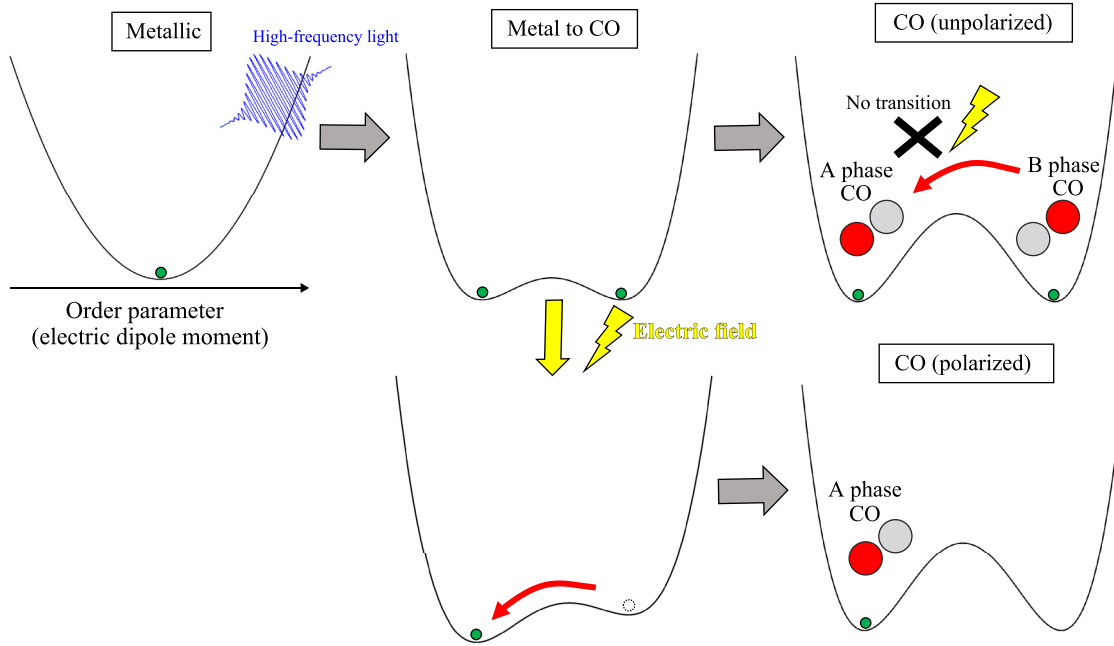


FIG. 11. Schematic diagram of the transition dynamics.

to the polarization direction of these two CO states, the two states have nearly the same weights, and the values of $|\Delta\rho_n(t)|$ when the THz pulse is polarized along the c axis are much smaller than the corresponding values when the THz pulse is polarized along the a axis. The polarization can thus be induced efficiently using the a -axis polarized THz pulse. We have calculated the dynamics when the dimer Mott insulator ground state is excited by the THz pulse (the light and THz pulses), and the temporal variations of $\Delta\rho_n(t)$ are shown in Fig. 13(a) [Fig. 13(b)]. The electronic parameters that give the dimer Mott insulator ground state are as follows: $\beta_{b1}^{(0)} = 0.275$, $\beta_{b2}^{(0)} = 0.070$, $\beta_p^{(0)} = 0.109$, $\beta_q^{(0)} = -0.038$, $U = 0.70$, $V_{b1} = 0.45$, $V_{b2} = V_p = 0.25$, and $V_q = 0.25$ [30]. We use the parameters for the light and THz pulses that are used to calculate the results shown in Fig. 10: $A_0^{(\max)} = 0.8 \text{ \AA}^{-1}$, $\mathbf{e}_0 \parallel a$, $D_0 = 60$, $\omega = 2.5$, $A_1^{(\max)} = 1.0 \text{ \AA}^{-1}$, $\mathbf{e}_1 \parallel a$, and $D_1 = 60$.

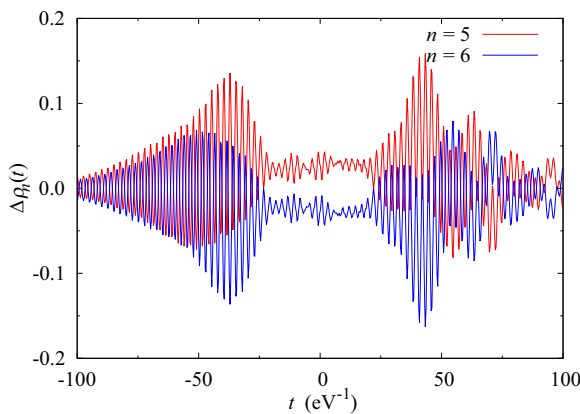


FIG. 12. Temporal variations in $\Delta\rho_n(t)$ for $n = 5$ and 6 induced by single light and THz pulses when $A_0^{(\max)} = 0.8 \text{ \AA}^{-1}$, $\mathbf{e}_0 \parallel a$, $D_0 = 60$, $\omega = 2.5$, $A_1^{(\max)} = 1.0 \text{ \AA}^{-1}$, $\mathbf{e}_1 \parallel c$, and $D_1 = 60$.

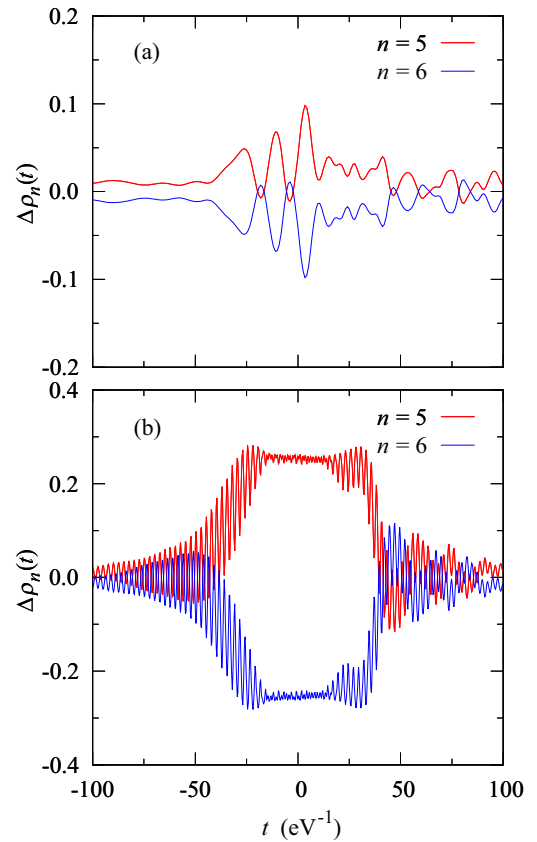


FIG. 13. (a) Temporal variations in $\Delta\rho_n(t)$ for $n = 5$ and 6 when the dimer Mott insulator ground state is excited by the THz pulse with $A_1^{(\max)} = 0 \text{ \AA}^{-1}$, $A_1^{(\max)} = 1.0 \text{ \AA}^{-1}$, $\mathbf{e}_1 \parallel a$, and $D_1 = 60$. (b) Corresponding variations when the dimer Mott insulator ground state is excited by the light and THz pulses with $A_0^{(\max)} = 0.8 \text{ \AA}^{-1}$, $\mathbf{e}_0 \parallel a$, $D_0 = 60$, $\omega = 2.5$, $A_1^{(\max)} = 1.0 \text{ \AA}^{-1}$, $\mathbf{e}_1 \parallel a$, and $D_1 = 60$.

When excited by the THz pulse, the charge correlations are nearly unaffected by the excitation process, and the photoinduced phase transition from the dimer Mott insulator to the CO state does not occur. As a result, $\Delta\rho_n(t)$ exhibits a complex oscillation, and the persistent and large polarization is not generated. This shows that the potential barrier between the dimer Mott insulator and the CO phases is so high that the transition cannot be induced by a THz pulse of feasible intensity.

When excited by the light and THz pulses, charge correlations characteristic of the CO phase are generated, and the photoinduced phase transition from the dimer Mott insulator to the CO state occurs. As a result, the persistent and large polarization is generated when the pulses are on, as seen in Fig. 13(b). Both the CO and dimer Mott insulator states are stabilized by the photoinduced reduction in the effective transfer integrals of the interdimer bonds (b2, p, and q bonds). However, that of the b1 bond stabilizes the CO state relative to the dimer Mott insulator state because only the dimer Mott insulator state is stabilized by the formation of the dimer (b1) bonds. As a result of the photoinduced reduction in $\tilde{\beta}_{b1}(t)$, the photoinduced phase transition from the dimer Mott insulator state to the CO state occurs. Similarly, the CO state is generated, but not the dimer Mott insulator state, in the metallic ground state case as a result of the photoinduced reduction in $\tilde{\beta}_{b1}(t)$.

D. Ultrafast polarization reversal

Taking the high potential barrier between the A phase and B phase CO states into consideration, we propose a scheme for ultrafast polarization reversal. Using double light and THz pulses, the phase transitions can be induced twice, and the pulse excited state can be changed in the sequence of metal \rightarrow A (B) phase CO state \rightarrow metal \rightarrow B (A) phase CO state. We then use the following double pulses:

$$\begin{aligned} A(t) = & A_0^{(\max)} e_0 \exp \left[-\left(\frac{t + d/2}{D_0} \right)^2 \right] \cos(\omega t) \\ & + A_0^{(\max)} e_0 \exp \left[-\left(\frac{t - d/2}{D_0} \right)^2 \right] \cos(\omega t) \\ & + \frac{A_1^{(\max)}}{2} e_1 \tanh \left[\left(\frac{t + d/2}{D_1} \right) \right] \\ & - \frac{A_1^{(\max)}}{2} e_1 \tanh \left[\left(\frac{t - d/2}{D_1} \right) \right], \end{aligned} \quad (23)$$

where d is the delay time between the first pair of pulses and the second pair of pulses. The first and second terms represent the first and second light pulses, respectively, and the third and fourth terms represent the first and second half-cycle THz pulses with opposite electric field directions, respectively. We use the following parameters for the double pulses: $A_0^{(\max)} = 0.8 \text{ \AA}^{-1}$, $A_1^{(\max)} = 0.5 \text{ \AA}^{-1}$, $D_0 = D_1 = 60$, and $d = 140$, and the temporal profiles of the electric fields of the light and THz pulses are shown in Fig. 14.

In Fig. 15, $\Delta\rho_n(t)$ is plotted for sites 5 and 6. Note that all the red (gray) sites shown in Fig. 5 are equivalent to site 5 (6) in the double pulse case. The polarized A phase CO

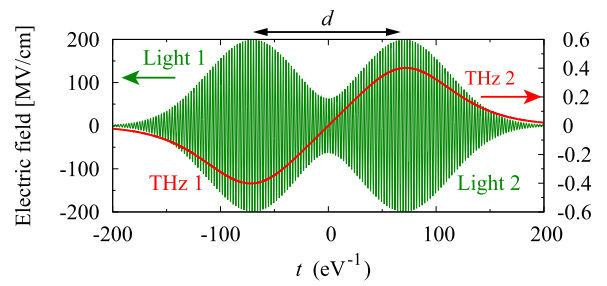


FIG. 14. Temporal profiles of the electric fields of the double light and THz pulses when $A_0^{(\max)} = 0.8 \text{ \AA}^{-1}$, $A_1^{(\max)} = 0.5 \text{ \AA}^{-1}$, $\omega = 2.5$, $D_0 = D_1 = 60$, and $d = 140$.

state is generated by the first pair of light and THz pulses. In the interval time region, the probability that a dimer is singly occupied $W_s(t)$ decreases almost to the probability for the metallic ground state, thus showing that the pulse-excited state changes into the metallic state. The signs of $\Delta\rho_n(t)$ are reversed, and the polarized B phase CO state is generated by the second pair of pulses, demonstrating that the polarization is reversed.

The magnitude of the charge order, which is given by $|\Delta\rho_n(t)|$, induced by the second pair of pulses is slightly smaller than that induced by the first pair of pulses. The reduction of the CO is attributed to the nonadiabatic nature of the transition, and this can be seen by referring to Fig. 8(b). In the case where $A^{(\max)} \leq 0.4 \text{ \AA}^{-1}$, where the phase transition does not occur, $W_s(t)$ returns almost to the value of the

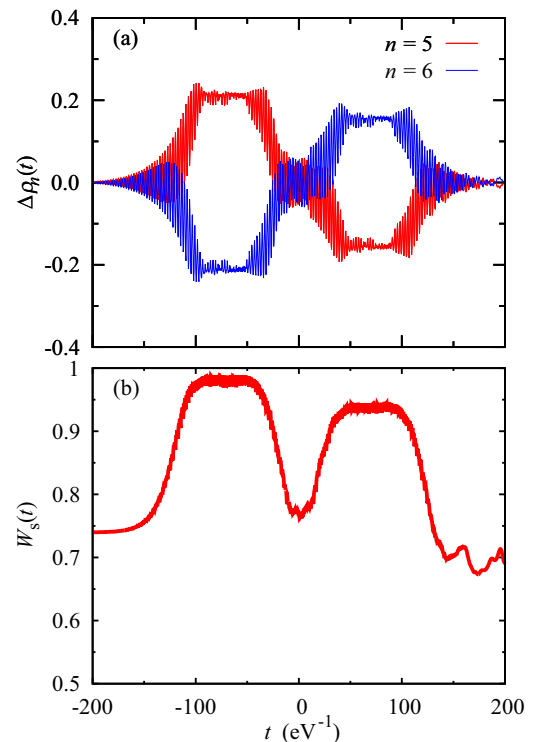


FIG. 15. Temporal variations in (a) $\Delta\rho_n(t)$ for $n = 5$ and 6 and (b) $W_s(t)$ induced by the double light and THz pulses when $A_0^{(\max)} = 0.8 \text{ \AA}^{-1}$, $A_1^{(\max)} = 0.5 \text{ \AA}^{-1}$, $\omega = 2.5$, $D_0 = D_1 = 60$, and $d = 140$.

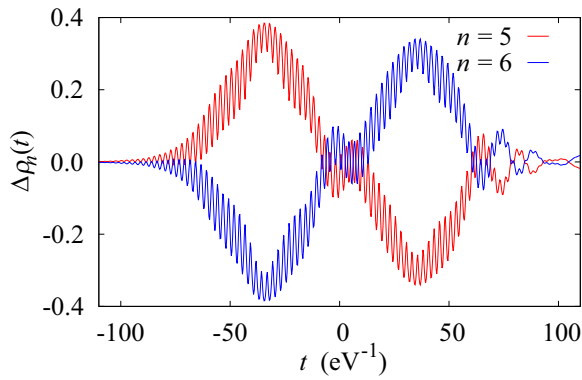


FIG. 16. Temporal variations in $\Delta\rho_n(t)$ for $n = 5$ and 6 induced by the double light and THz pulses when $A_0^{(\max)} = 0.6 \text{ \AA}^{-1}$, $A_1^{(\max)} = 1.0 \text{ \AA}^{-1}$, $D_0 = D_1 = 30$, and $d = 70$.

metallic ground state $W_s^{(M)}$ after the pulse is turned off. In the case where $A^{(\max)} \geq 0.6 \text{ \AA}^{-1}$, where the phase transition does occur, $W_s(t)$ deviates significantly from $W_s^{(M)}$ after the pulse is turned off. Because the transition is nonadiabatic, the electronic system absorbs energy during every transition process. Since we do not consider a heat bath in this case, the energy accumulates, and the deviation of $|\psi(t)\rangle$ from the ground state $|\phi_0(t)\rangle$ of the effective Hamiltonian increases over time. In a real system, the reduction of the charge order could be avoided if the energy transfer to the heat bath were made rapidly enough.

We have calculated the dynamics using various pulse parameters and have investigated how rapidly the polarization can be reversed. Figure 16 shows the results for the shorter time interval, with $A_0^{(\max)} = 0.6 \text{ \AA}^{-1}$, $A_1^{(\max)} = 1.0 \text{ \AA}^{-1}$, $D_0 = D_1 = 30$, and $d = 70$. The values of the pulse-induced charges $\Delta\rho_n(t)$ do not remain nearly constant, but the peaks of $|\Delta\rho_n(t)|$ occur at the peak times $\pm d/2$ for the double pulses. Therefore, the polarization can be controlled and reversed using the double pulses. This shows that polarization can be reversed on a timescale of several tens of femtoseconds by manipulating the optimal pulses.

IV. DISCUSSION

It is difficult to investigate the system size dependence of the photoinduced dynamics because of the difficulty of performing numerical calculations on large systems. In the numerical calculations presented here, which are based on a small cluster, it is shown that the homogeneous CO phase is generated by photoexcitation. However, CO phase domains are believed to form, rather than homogeneous phase formation occurring in the thermodynamic limit. The domain formation is an important problem, but it lies beyond the scope of this study.

It was reported previously that an intensity of $2.2 \times 10^{12} \text{ V/cm}$ was achieved with a laser with a photon energy of approximately 3 eV [89], and the intensity of the THz pulse can reach 1 MV/cm [90,91]. In the numerical calculations here, photoinduced phase transitions to the CO phase and ultrafast polarization reversal occur even at intensities that are much smaller than these realizable intensities. We consider the

most serious problem with regard to experimental feasibility to be finding the photon energy range window. The photon energy of 3 eV is off resonant in the present model, but in real materials, there may be excited states with energies of around 3 eV that arise from degrees of freedom that have not been considered in the model. Excitation of these irrelevant modes generates heat, and the resulting increase in temperature may destroy the charge order.

The SHG process becomes active when the polarization is formed and the inversion symmetry is broken. Therefore, terahertz-pump SHG-probe measurements have been demonstrated to be a powerful tool for investigation of ultrafast dielectric responses [38,39]. The second-harmonic (SH) waves from the polarized phases with antiparallel polarizations are out of phase. Therefore, the polarization direction of a sample can be determined from the phase of the SH wave, and the phase can be obtained by making the SH wave from the sample interfere with that from a reference material with a known polarization direction. The polarization reversal can be detected from the interference of the SH waves.

V. CONCLUSION

We have theoretically investigated the dynamics induced by higher-frequency off-resonant light pulse excitation in the metallic phase of κ -(BEDT-TTF)₂X by numerically solving the TDSE in the quarter-filled extended Hubbard model for the material. For $A^{(\max)} \gtrsim 0.6 \text{ \AA}^{-1}$ and $\omega \gtrsim 2.0$, the transition to the CO state, in which one site forming a dimer becomes charge rich, the other site becomes charge poor, and the intradimer electric dipole moments are aligned along the a axis, is induced by light pulse excitation. The transition is transient, and the pulse excited state gets close to the metallic ground state after the pulse is turned off. The transition is driven by photoinduced reduction of the effective transfer integrals, and the transition is therefore the result of dynamical localization. The photogenerated CO state is given by the superposition of two degenerate A phase and B phase CO states with opposite polarization directions and equal weights, and the polarization of the CO state is effectively zero. The transitions to either of the two polarized CO states can be induced selectively, and the polarization can be generated by excitation using light and the a -axis polarized THz pulses. Furthermore, the polarization can be reversed on a timescale of several tens of femtoseconds via excitation using double light and THz pulses, where the electric fields of the two THz pulses are oriented in opposite directions. The first pair of pulses induces the transition from the metallic ground state to the polarized CO state of the A (B) phase. After the first pulse is turned off and the pulse excited states return to the metallic state, the material is irradiated by the second pair of pulses, and the transition from the metallic state to the polarized CO state of the B (A) phase is induced.

ACKNOWLEDGMENT

This work was supported by Core Research for Evolutional Science and Technology, Japan Science and Technology Agency (JST CREST) in Japan (Grant No. JPMJCR1661).

- [1] K. Uchino, *Ferroelectric Devices* (Dekker, New York 2000).
- [2] M. E. Lines and A. M. Glass, *Principles and Applications of Ferroelectrics and Related Materials* (Oxford University Press, New York, 1977).
- [3] J. F. Scott, *Science* **315**, 954 (2007).
- [4] T. Portengen, Th. Östreich, and L. J. Sham, *Phys. Rev. B* **54**, 17452 (1996).
- [5] J. van den Brink and D. I. Khomskii, *J. Phys.: Condens. Matter* **20**, 434217 (2008).
- [6] S. Ishihara, *J. Phys. Soc. Jpn.* **79**, 011010 (2010).
- [7] T. Kimura, T. Goto, H. Shintani, K. Ishizaka, T. Arima, and Y. Tokura, *Nature (London)* **426**, 55 (2003).
- [8] J. Wang, J. B. Neaton, H. Zheng, V. Nagarajan, S. B. Ogale, B. Liu, D. Viehland, V. Vaithyanathan, D. G. Schlom, U. V. Waghmare, N. A. Spaldin, K. M. Rabe, M. Wuttig, and R. Ramesh, *Science* **299**, 1719 (2003).
- [9] N. A. Spaldin and M. Fiebig, *Science* **309**, 391 (2005).
- [10] W. Eerenstein, N. D. Mathur, and J. F. Scott, *Nature (London)* **442**, 759 (2006).
- [11] S.-W. Cheong and M. Mostovoy, *Nat. Mater.* **6**, 13 (2007).
- [12] S. Picozzi, K. Yamauchi, B. Sanyal, I. A. Sergienko, and E. Dagotto, *Phys. Rev. Lett.* **99**, 227201 (2007).
- [13] D. Khomskii, *Physics* **2**, 20 (2009).
- [14] P. Lunkenheimer, J. Müller, S. Krohns, F. Schrettle, A. Loidl, B. Hartmann, R. Rommel, M. de Souza, C. Hotta, J. A. Schlueter, and M. Lang, *Nat. Mater.* **11**, 755 (2012).
- [15] N. Ikeda, H. Ohsumi, K. Ohwada, K. Ishii, T. Inami, K. Kakurai, Y. Murakami, K. Yoshii, S. Mori, Y. Horibe, and H. Kito, *Nature (London)* **436**, 1136 (2005).
- [16] A. Nagano, M. Naka, J. Nasu, and S. Ishihara, *Phys. Rev. Lett.* **99**, 217202 (2007).
- [17] M. Naka, A. Nagano, and S. Ishihara, *Phys. Rev. B* **77**, 224441 (2008).
- [18] K. Kobayashi, S. Horiuchi, R. Kumai, F. Kagawa, Y. Murakami, and Y. Tokura, *Phys. Rev. Lett.* **108**, 237601 (2012).
- [19] G. Giovannetti, S. Kumar, A. Stroppa, J. van den Brink, and S. Picozzi, *Phys. Rev. Lett.* **103**, 266401 (2009).
- [20] S. Ishibashi and K. Terakura, *Physica B (Amsterdam, Neth.)* **405**, S338 (2010).
- [21] S. Ishibashi and K. Terakura, *J. Phys. Soc. Jpn.* **83**, 073702 (2014).
- [22] K. Terakura and S. Ishibashi, *Phys. Rev. B* **91**, 195120 (2015).
- [23] P. Monceau, F. Ya. Nad, and S. Brazovskii, *Phys. Rev. Lett.* **86**, 4080 (2001).
- [24] H. Yoshioka, M. Tsuchiizu, and H. Seo, *J. Phys. Soc. Jpn.* **76**, 103701 (2007).
- [25] Y. Otsuka, H. Seo, Y. Motome, and T. Kato, *J. Phys. Soc. Jpn.* **77**, 113705 (2008).
- [26] K. Yamamoto, S. Iwai, S. Boyko, A. Kashiwazaki, F. Hiramatsu, C. Okabe, N. Nishi, and K. Yakushi, *J. Phys. Soc. Jpn.* **77**, 074709 (2008).
- [27] K. Yamamoto, A. Kowalska, and K. Yakushi, *Appl. Phys. Lett.* **96**, 122901 (2010).
- [28] P. Lunkenheimer, B. Hartmann, M. Lang, J. Müller, D. Schweitzer, S. Krohns, and A. Loidl, *Phys. Rev. B* **91**, 245132 (2015).
- [29] M. Abdel-Jawad, I. Terasaki, T. Sasaki, N. Yoneyama, N. Kobayashi, Y. Uesu, and C. Hotta, *Phys. Rev. B* **82**, 125119 (2010).
- [30] H. Gomi, T. Imai, A. Takahashi, and M. Aihara, *Phys. Rev. B* **82**, 035101 (2010).
- [31] M. Naka and S. Ishihara, *J. Phys. Soc. Jpn.* **79**, 063707 (2010).
- [32] C. Hotta, *Phys. Rev. B* **82**, 241104(R) (2010).
- [33] S. Dayal, R. T. Clay, H. Li, and S. Mazumdar, *Phys. Rev. B* **83**, 245106 (2011).
- [34] K. Itoh, H. Itoh, M. Naka, S. Saito, I. Hosako, N. Yoneyama, S. Ishihara, T. Sasaki, and S. Iwai, *Phys. Rev. Lett.* **110**, 106401 (2013).
- [35] M. Naka and S. Ishihara, *J. Phys. Soc. Jpn.* **82**, 023701 (2013).
- [36] H. Gomi, M. Ikenaga, Y. Hiragi, D. Segawa, A. Takahashi, T. J. Inagaki, and M. Aihara, *Phys. Rev. B* **87**, 195126 (2013).
- [37] H. Gomi, T. J. Inagaki, and A. Takahashi, *Phys. Rev. B* **93**, 035105 (2016).
- [38] T. Miyamoto, H. Yada, H. Yamakawa, and H. I. Okamoto, *Nat. Commun.* **4**, 2586 (2013).
- [39] H. Yamakawa, T. Miyamoto, T. Morimoto, H. Yada, Y. Kinoshita, M. Sotome, N. Kida, K. Yamamoto, K. Iwano, Y. Matsumoto, S. Watanabe, Y. Shimoi, M. Suda, H. M. Yamamoto, H. Mori, and H. Okamoto, *Sci. Rep.* **6**, 20571 (2016).
- [40] H. Gomi, N. Yamagishi, T. Mase, T. J. Inagaki, and A. Takahashi, *Phys. Rev. B* **95**, 094116 (2017).
- [41] S. Kuniki, S. Ohmura, and A. Takahashi, *Phys. Rev. B* **98**, 165149 (2018).
- [42] T. Morimoto, T. Miyamoto, H. Yamakawa, T. Terashige, T. Ono, N. Kida, and H. Okamoto, *Phys. Rev. Lett.* **118**, 107602 (2017).
- [43] H. Yamakawa, T. Miyamoto, T. Morimoto, N. Takamura, S. Liang, H. Yoshimochi, T. Terashige, N. Kida, M. Suda, H. M. Yamamoto, H. Mori, K. Miyagawa, K. Kanoda, and H. Okamoto, *Nat. Commun.* **12**, 953 (2021).
- [44] X. Li, T. Qiu, J. Zhang, E. Baldini, J. Lu, A. M. Rappe, and K. A. Nelson, *Science* **364**, 1079 (2019).
- [45] T. F. Nova, A. S. Disa, M. Fechner, and A. Cavalleri, *Science* **364**, 1075 (2019).
- [46] S. Ohmura, T. Mase, and A. Takahashi, *Phys. Rev. B* **100**, 035116 (2019).
- [47] Y. Tokura, *J. Phys. Soc. Jpn.* **75**, 011001 (2006).
- [48] K. Yonemitsu and K. Nasu, *J. Phys. Soc. Jpn.* **75**, 011008 (2006).
- [49] K. Yonemitsu and K. Nasu, *Phys. Rep.* **465**, 1 (2008).
- [50] K. Nasu, *Eur. Phys. J. B* **75**, 415 (2010).
- [51] D. N. Basov, R. D. Averitt, D. van der Marel, M. Dressel, and K. Haule, *Rev. Mod. Phys.* **83**, 471 (2011).
- [52] H. Matsuzaki, M. Iwata, T. Miyamoto, T. Terashige, K. Iwano, S. Takaishi, M. Takamura, S. Kumagai, M. Yamashita, R. Takahashi, Y. Wakabayashi, and H. Okamoto, *Phys. Rev. Lett.* **113**, 096403 (2014).
- [53] L. Rettig, R. Cortés, J.-H. Chu, I. R. Fisher, F. Schmitt, R. G. Moore, Z.-X. Shen, P. S. Kirchmann, M. Wolf, and U. Bovensiepen, *Nat. Commun.* **7**, 10459 (2016).
- [54] A. Singer, S. K. K. Patel, R. Kukreja, V. Uhlir, J. Wingert, S. Festersen, D. Zhu, J. M. Glownia, H. T. Lemke, S. Nelson, M. Kozina, K. Rossnagel, M. Bauer, B. M. Murphy, O. M. Magnussen, E. E. Fullerton, and O. G. Shpyrko, *Phys. Rev. Lett.* **117**, 056401 (2016).
- [55] K. W. Kim, A. Pashkin, H. Schäfer, M. Beyer, M. Porer, T. Wolf, C. Bernhard, J. Demsar, R. Huber, and A. Leitenstorfer, *Nat. Mater.* **11**, 497 (2012).

- [56] A. Takahashi, H. Gomi, and M. Aihara, *Phys. Rev. B* **66**, 115103 (2002).
- [57] D. Fausti, R. I. Tobey, N. Dean, S. Kaiser, A. Dienst, M. C. Hoffmann, S. Pyon, T. Takayama, H. Takagi, and A. Cavalleri, *Science* **331**, 189 (2011).
- [58] D. Nicoletti and A. Cavalleri, *Adv. Opt. Photonics* **8**, 401 (2016).
- [59] K. Onda, S. Ogihara, K. Yonemitsu, N. Maeshima, T. Ishikawa, Y. Okimoto, X. Shao, Y. Nakano, H. Yamochi, G. Saito, and S. Y. Koshihara, *Phys. Rev. Lett.* **101**, 067403 (2008).
- [60] L. Guérin, J. Hébert, M. Buron-LeCointe, S. I. Adachi, S. Y. Koshihara, H. Cailleau, and E. Collet, *Phys. Rev. Lett.* **105**, 246101 (2010).
- [61] M. Servol, N. Moisan, E. Collet, H. Cailleau, W. Kaszub, L. Toupet, D. Boschetto, T. Ishikawa, A. Moréac, S. Koshihara, M. Maesato, M. Uruichi, X. Shao, Y. Nakano, H. Yamochi, G. Saito, and M. Lorenc, *Phys. Rev. B* **92**, 024304 (2015).
- [62] T. Ishikawa, Y. Sagae, Y. Naitoh, Y. Kawakami, H. Itoh, K. Yamamoto, K. Yakushi, H. Kishida, T. Sasaki, S. Ishihara, Y. Tanaka, K. Yonemitsu, and S. Iwai, *Nat. Commun.* **5**, 5528 (2014).
- [63] Y. Kawakami, Y. Yoneyama, T. Amano, H. Itoh, K. Yamamoto, Y. Nakamura, H. Kishida, T. Sasaki, S. Ishihara, Y. Tanaka, K. Yonemitsu, and S. Iwai, *Phys. Rev. B* **95**, 201105(R) (2017).
- [64] D. H. Dunlap and V. M. Kenkre, *Phys. Rev. B* **34**, 3625 (1986).
- [65] F. Grossmann, T. Dittrich, P. Jung, and P. Hänggi, *Phys. Rev. Lett.* **67**, 516 (1991).
- [66] Y. Kayanuma, *Phys. Rev. A* **50**, 843 (1994).
- [67] Y. Naitoh, Y. Kawakami, T. Ishikawa, Y. Sagae, H. Itoh, K. Yamamoto, T. Sasaki, M. Dressel, S. Ishihara, Y. Tanaka, K. Yonemitsu, and S. Iwai, *Phys. Rev. B* **93**, 165126 (2016).
- [68] K. Yonemitsu, *J. Phys. Soc. Jpn.* **86**, 024711 (2017).
- [69] K. Yonemitsu, *J. Phys. Soc. Jpn.* **86**, 064702 (2017).
- [70] K. Oya and A. Takahashi, *Phys. Rev. B* **97**, 115147 (2018).
- [71] N. Tsuji, T. Oka, P. Werner, and H. Aoki, *Phys. Rev. Lett.* **106**, 236401 (2011).
- [72] N. Tsuji, T. Oka, H. Aoki, and P. Werner, *Phys. Rev. B* **85**, 155124 (2012).
- [73] K. Yonemitsu and K. Nishioka, *J. Phys. Soc. Jpn.* **84**, 054702 (2015).
- [74] H. Yanagiya, Y. Tanaka, and K. Yonemitsu, *J. Phys. Soc. Jpn.* **84**, 094705 (2015).
- [75] A. Ono, H. Hashimoto, and S. Ishihara, *Phys. Rev. B* **94**, 115152 (2016).
- [76] A. Ono, H. Hashimoto, and S. Ishihara, *Phys. Rev. B* **95**, 085123 (2017).
- [77] H. Kino and H. Fukuyama, *J. Phys. Soc. Jpn.* **64**, 2726 (1996).
- [78] H. Kino and H. Fukuyama, *J. Phys. Soc. Jpn.* **65**, 2158 (1996).
- [79] H. C. Kandpal, I. Opahle, Y.-Z. Zhang, H. O. Jeschke, and R. Valentí, *Phys. Rev. Lett.* **103**, 067004 (2009).
- [80] K. Nakamura, Y. Yoshimoto, T. Kosugi, R. Arita, and M. Imada, *J. Phys. Soc. Jpn.* **78**, 083710 (2009).
- [81] K. Sedlmeier, S. Elsässer, D. Neubauer, R. Beyer, D. Wu, T. Ivek, S. Tomić, J. A. Schlueter, and M. Dressel, *Phys. Rev. B* **86**, 245103 (2012).
- [82] M. Pinterić, M. Čulo, O. Milat, M. Basletić, B. Korin-Hamzić, E. Tafra, A. Hamzić, T. Ivek, T. Peterseim, K. Miyagawa, K. Kanoda, J. A. Schlueter, M. Dressel, and S. Tomić, *Phys. Rev. B* **90**, 195139 (2014).
- [83] S. Tomić, M. Pinterić, T. Ivek, K. Sedlmeier, R. Beyer, D. Wu, J. A. Schlueter, D. Schweitzer, and M. Dressel, *J. Phys.: Condens. Matter* **25**, 436004 (2013).
- [84] M. Pinterić, T. Ivek, M. Čulo, O. Milat, M. Basletić, B. Korin-Hamzić, E. Tafra, A. Hamzić, M. Dressel, and S. Tomić, *Physica B (Amsterdam, Neth.)* **460**, 202 (2015).
- [85] K. G. Padmalekha, M. Blankenhorn, T. Ivek, L. Bogani, J. A. Schlueter, and M. Dressel, *Physica B (Amsterdam, Neth.)* **460**, 211 (2015).
- [86] T. Mori, H. Mori, and S. Tanaka, *Bull. Chem. Soc. Jpn.* **72**, 179 (1999).
- [87] D. Faltermeier, J. Barz, M. Dumm, M. Dressel, N. Drichko, B. Petrov, V. Semkin, R. Vlasova, C. Mezière, and P. Batail, *Phys. Rev. B* **76**, 165113 (2007).
- [88] M. Dumm, D. Faltermeier, N. Drichko, M. Dressel, C. Mezière, and P. Batail, *Phys. Rev. B* **79**, 195106 (2009).
- [89] Y. Wang, S. N. Wang, A. Rockwood, B. M. Luther, R. Hollinger, A. Curtis, C. Calvi, C. S. Menoni, and J. J. Rocca, *Opt. Lett.* **42**, 3828 (2017).
- [90] J. Hebling, G. Almási, I. Z. Kozma, and J. Kuhl, *Opt. Express* **10**, 1161 (2002).
- [91] H. Hirori, K. Shinokita, M. Shirai, S. Tani, and Y. Kadoya, *Nat. Commun.* **2**, 594 (2011).